


RESEARCH

Open Access



Multi-omics evaluation of clinical-grade human umbilical cord-derived mesenchymal stem cells in synergistic improvement of aging related disorders in a senescence-accelerated mouse model

Jiabian Lian^{1,2,3†}, Lu Xia^{1,2,3*†} , Guohao Wang^{1†}, Weijing Wu⁴, Ping Yi⁴, Meilin Li⁴, Xufeng Su⁴, Yushuo Chen⁴, Xun Li^{2,3*}, Fei Dou^{5,6*} and Zhanxiang Wang^{1,7*}

Abstract

Background The prevalence of age-related disorders, particularly in neurological and cardiovascular systems, is an increasing global health concern. Mesenchymal stem cell (MSC) therapy, particularly using human umbilical cord-derived MSCs (HUCMSCs), has shown promise in mitigating these disorders. This study investigates the effects of HUCMSCs on aging-related conditions in a senescence-accelerated mouse model (SAMP8), with a focus on DNA damage, gut microbiota alterations, and metabolic changes.

Methods SAMP8 mice were treated with clinical-grade HUCMSCs via intraperitoneal injections. Behavioral and physical assessments were conducted to evaluate cognitive and motor functions. The Single-Strand Break Mapping at Nucleotide Genome Level (SSiNGLe) method was employed to assess DNA single-strand breaks (SSBs) across the genome, with particular attention to exonic regions and transcription start sites. Gut microbiota composition was analyzed using 16S rRNA sequencing, and carboxyl metabolomic profiling was performed to identify changes in circulating metabolites.

Results HUCMSC treatment significantly improved motor coordination and reduced anxiety in SAMP8 mice. SSiNGLe analysis revealed a notable reduction in DNA SSBs in MSC-treated mice, especially in critical genomic regions, suggesting that HUCMSCs may mitigate age-related DNA damage. The functional annotation of the DNA breakome indicated a potential link between reduced DNA damage and altered metabolic pathways. Additionally, beneficial

[†]Jiabian Lian, Lu Xia, and Guohao Wang are co-first authors of this manuscript.

*Correspondence:

Lu Xia

Luxia@xmu.edu.cn

Xun Li

xli2001@xmu.edu.cn

Fei Dou

douf@bnu.edu.cn

Zhanxiang Wang

wangzx@xmu.edu.cn

Full list of author information is available at the end of the article



alterations in gut microbiota were observed, including an increase in short-chain fatty acid (SCFA)-producing bacteria, which correlated with improved metabolic profiles.

Conclusion The administration of HUCMSCs in SAMP8 mice not only reduces DNA damage but also induces favorable changes in gut microbiota and metabolism. The observed alterations in DNA break patterns, along with specific changes in microbiota and metabolic profiles, suggest that these could serve as potential biomarkers for evaluating the efficacy of HUCMSCs in treating age-related disorders. This highlights a promising avenue for the development of new therapeutic strategies that leverage these biomarkers, to enhance the effectiveness of HUCMSC-based treatments for aging-associated diseases.

Keywords Faecal microbiome, Metabolomics, Human umbilical cord mesenchymal stem cells, Senescence-accelerated mouse model, Aging, DNA breaks

Introduction

Globally, as life expectancy increases, the prevalence of age-related pathologies, particularly neurological and cardiovascular diseases, has grown, placing substantial burdens on healthcare and social systems. Advancing age can increase the risk of dementia due to shared risk factors with heart failure (HF), which significantly diminishes quality of life [1]. The senescence-accelerated mouse-prone 8 (SAMP8) model offers an excellent paradigm for studying Alzheimer's disease and heart failure within the aging context. These mice effectively replicate human aging phenomena, providing a pertinent model for studying Gerosuppressive drugs [2].

Mesenchymal stem cells (MSCs) are noted for their self-renewal capabilities and ability to differentiate into a variety of cell types. Increasing evidence points to the therapeutic effects of MSCs being primarily mediated by paracrine actions, particularly through secretory factors such as exosomes [3]. Furthermore, human umbilical cord-derived MSCs (HUCMSCs) have shown the ability to ameliorate colon inflammation by modulating the gut microbiota-short-chain fatty acids-immune axis [4], indicating potential modulatory effects on the gut-brain and gut-heart axes with implications for aging.

This study demonstrates that intraperitoneal administration of HUCMSCs in SAMP8 mice improves curiosity, motor coordination, balance, and reduces fearfulness. Additionally, this treatment mitigates organ degeneration throughout the body. Notably, changes in the gut microbial profile, associated with metabolic alterations, underscore the systemic benefits of MSC treatment in this aging model. Our findings propose that targeting gut-organ axis mechanisms of aging via MSC therapy could provide promising pathways for extending health span and alleviating age-related disorders.

Materials and methods

Clinical-grade HUCMSCs preparation

We utilized clinical-grade human umbilical cord mesenchymal stem cells (HUCMSCs), which underwent rigorous optimization. Clinical-grade HUCMSCs (YFQLXB-UC01) were generously provided by Shandong Qilu Cell Therapy Engineering Technology Co., Ltd., and prepared using the following method: The solvent was prepared by diluting physiological saline with the solvent in a 4:1 ratio. Once the water bath temperature was stable, cells were retrieved from the liquid nitrogen tank. The aluminum cryostorage box was opened, and the cryovial was quickly removed and placed in the 37 °C water bath, gently agitating for approximately 1 min until the cells thawed. The exterior of the cryovial was disinfected with 75% ethanol before transferring to the biological safety cabinet. The luer lock cap of the cryovial was snapped off, and using a 10 ml syringe, the cell suspension was drawn out and transferred into a 15 ml centrifuge tube. Approximately 20 ml of the prepared solvent was added to a separate 50 ml centrifuge tube. An appropriate volume of the cell suspension was added to the solvent-containing tube, capped, inverted gently to mix, and then centrifuged at 300 g for 5 min. After centrifugation, the 50 ml centrifuge tube was carefully removed to avoid disturbing the pellet. The supernatant was aspirated, and the tube was gently agitated to loosen the cell pellet. A sufficient volume of solvent was added to resuspend the cells, ensuring uniform suspension by gently pipetting up and down. A 70 µm cell strainer was placed onto a new 50 ml centrifuge tube using forceps, and the resuspended cell solution was poured through the strainer to filter the cells. The filtered cell suspension was counted using a Countstar automated cell counter, and based on the cell count results, the concentration was adjusted to the target value by adding either more solvent or additional cell suspension. Besides, basic characteristics of HUCMSCs was verified (Figure S1, Supplementary materials and methods). In all experiments, the

generation of HUCMSCs was limited from passage 3 (P3) to passage 5 (P5).

Animals and treatment

The work has been reported in line with the ARRIVE guidelines 2.0. We acquired senescence-accelerated mouse prone 8 (SAMP8, $n=30$) and senescence-accelerated mouse resistant 1 (SAMR1, $n=15$) from Peking University Health Science Center. In contrast to SAMP8, the SAMR1 strain serves as a control model representing normal aging. Four-month-old male SAMP8 and SAMR1 mice were used. The animals were housed at the Xiamen University Experimental Animal Center (SPF grade) and were given at least one week to acclimate before the stem cell injection experiments. Randomisation was used to allocate experimental units to control and treatment groups. In block randomization, the SAMP8 experimental animals were grouped into 3 blocks based on their body weight. Within each block, the animals were then randomly assigned to different experimental groups. This approach ensures that each experimental group remains balanced in terms of these characteristics. To minimize potential confounders such as the order of treatments and measurements, a fixed ear tag sequence was applied. The vehicle-treated mice received 500 μL of phosphate-buffered saline (PBS) ($n=15$). The SAMP8 mice received intraperitoneal injections of 5×10^6 HUCMSCs in 500 μL PBS weekly for eight weeks ($n=15$), while the SAMR1 mice received 500 μL of PBS served as the control group ($n=15$). The average body weight of these 4-month-old SAMP8/R1 mice was approximately 32 g. All animals were cared for in accordance with the Guide for the Care and Use of Laboratory Animals, under a protocol approved by the Laboratory Animal Management and Ethics Committee of Xiamen University (Approval No. XMULAC20220056, date of approval: 07/04/2022). The criteria for exclusion was sample abnormality and data outlier. Only the personnel responsible for tagging, administering medication, and final data analysis were aware of the group assignments. Other experimenters conducted their tasks solely based on the ear tag numbers to ensure the blindness of the experimental process.

Plasma and fecal collection

One week after the final administration of the treatment to 6-month-old mice, fecal and blood samples were collected.

Fecal sample collection Each mouse was placed in a plastic basket lined with filter paper. Only one mouse was placed in each basket. Fresh feces were collected within 2 h and placed into 2 mL cryovials.

Blood plasma collection All animals were anesthetized using isoflurane inhalation. 100 μL of blood was drawn

from the tail vein. The blood samples were centrifuged at 3500 rpm for 8 min to separate the plasma. The plasma was then used for subsequent metabolomics experiments. These procedures ensure the collection of high-quality samples for accurate and reliable metabolomics analysis.

Assessment of neuro and physical function of senescence accelerated mice

In all senescence accelerated models, mice were checked twice per week for body weight. Before conducting the following behavioral experiments, the mice were transferred from their housing environment to the experimental room, where they were given a 2-h acclimation period.

Novel object recognition task The novel object recognition task evaluates recognition memory. In the novel object recognition task, the mice were placed in an empty testing box for 5 min to adapt. During the familiarization phase, objects A and B were symmetrically placed on the same side of the box, 10 cm from the wall. The first batch of mice was released from the opposite midpoint facing the wall, and allowed to freely explore for 5 min. In the test phase, object B was replaced with object C, and the first batch of mice was again released from the opposite midpoint facing the wall for another 5 min of free exploration. After each animal's trial, they were temporarily placed in an empty cage until all mice in the group had completed their trials, after which they were returned to their original cages. After each animal's experiment, the equipment was cleaned with 75% ethanol and aired out for 10 s to prevent odor residue. Exploration time with the novel object is the primary outcome measure. One outlier was removed from the SAMP8-PBS group in the Novel Object Recognition Test.

Elevated plus maze The elevated plus maze assesses anxiety-like behavior. The elevated plus maze consists of two open arms and two enclosed arms, arranged in a plus-shaped configuration. Animals were placed in the center of the maze and allowed to freely explore for 5 min. The time spent in the open arms and the closed arms was measured, serving as a proxy for anxiety-like behavior, with decreased time in the open arms reflecting increased anxiety.

Rotarod task The rotarod task assesses motor coordination and balance in animals, which were conducted using a device with a rod diameter of 30 mm and a length of 60 mm. Prior to the official test, mice were placed on the rotarod device and trained for 10 min at a speed of 20 r/min. During the official test, the parameters were set to 300 s, with an initial speed of 5 r/min, increasing to 40 r/min over approximately 2 min. Each mouse was tested three times, with a 30-min interval between each trial.

The latency to fall (time to fall) and the speed at the time of falling were recorded, and the average of three trials was calculated. After each mouse's test, the apparatus was cleaned of mouse excrement and wiped with 75% alcohol to eliminate residual odors, preventing interference with subsequent tests. Longer latencies and higher speeds are indicative of better motor coordination and balance.

We conducted the experiment with a maximum of 7–8 mice per group in the following experiments according to the resource equation approach [5]. Taking into account the significant physical exertion required for behavioral tests, the animal behavior experiment was conducted in two batches: one batch for the object recognition test and Morris water maze (data not shown), and another batch for the elevated plus maze and rotarod test. The specific sample size of each task was specified in the figure legends of Fig. 1.

Assessment of pathological feature of senescence accelerated mice

The mice were sacrificed after anesthesia by carbon dioxide. The dissected tissues (brain, heart, lung, skeletal muscle, liver, spleen, kidney, and colon) were fixed in 4% formalin for 48 h, then embedded in paraffin and sectioned into 4- μ m slides, and stained according to Servicebio's standard operating procedures ($n=8$ per group). All sections were first deparaffinized in Servicebio's Environmental Friendly Dewaxing Liquid for 40 min (20 min each in type I and II solutions) and rehydrated through a series of ethanol solutions (100%, 100%, 95%) for a total of 15 min.

Hematoxylin and Eosin (H and E) staining were applied using H and E HD constant dye kit (Servicebio# G1076, China) to evaluate histopathological impairment. Sections were stained with hematoxylin for 3–5 min, differentiated with differentiation solution, and then blued. Eosin was applied for 15 s after dehydration steps using ethanol and normal butanol. The slides were cleared in xylene and mounted with neutral gum (SCRC#10,004,160, China). Nissl staining was applied to reflect neuronal resilience and protein synthesis: Sections were stained with toluidine blue (Servicebio#G1032) for 2–5 min, differentiated with 0.1% glacial acetic acid (SCRC#10,000,218), and rinsed in tap water to stop the reaction. Slides were dried in an oven. Microscopy and imaging analysis was performed using a Nikon ECLIPSE E100 upright optical microscope, equipped with a DS-U3 imaging system. Images were acquired and processed for detailed histopathological evaluation.

SSiNGLe(single-strand break mapping at nucleotide genome level) method

Both DNA single-strand breaks (SSBs) and double-strand breaks (DSBs) can be detected using the SSiNGLe method (hereafter referred to as SSBs for both types). The dissected brain tissue was snap-frozen and subjected to DNA extraction according to the manufacturer's instructions (Xi'an Tianlong Science and Technology Co., Ltd#T093). The DNA library was constructed as described in the previous article [6]. The relative abundance (RA) of SSB in each sample was calculated using the following formula:

$$RA = \frac{\text{SSB counts in the indicated region of the current sample}}{\frac{\text{Total SSB counts of all samples}}{\text{Total sample number}}}$$

(See figure on next page.)

Fig. 1 HUCMSCs improved phenotype of mental and physical healthiness in SAMP8 Mice. **A** Schematic diagram of experimental design **B** New Object recognition test ($n=8$ per group). **C** Rotarod test was applied to analyze drop time and drop speed ($n=7$ per group). **D** Elevated plus maze was applied to analyze time in zone and entries in zone between group, and the percentage of entries in open arm and the percentage of time in open arm ($n=7$ per group). **E** The body weight was measured twice a week ($n=8-15$ per group). **F** Genome-wide analysis of DNA single-strand breaks (SSBs) in different experimental groups. The bar graphs show the SSB levels in the whole genome, exonic regions, and within 200 bp of transcription start sites (TSS) for the P8_P, R1_P, and P8_M groups ($n=6-7$ per group). **G** Gene clusters with the top 20 KEGG and Reactome pathways. The KEGG pathways of Exon_1 only returned 13 terms. All data shown as mean \pm SD. Data were analyzed using one-way ANOVA followed by Tukey's post-hoc test in subfigure B-D and F. Abbreviation: R1_P: SAMR1_PBS; P8_P: SAMP8_PBS; and P8_M: SAMP8_MSC

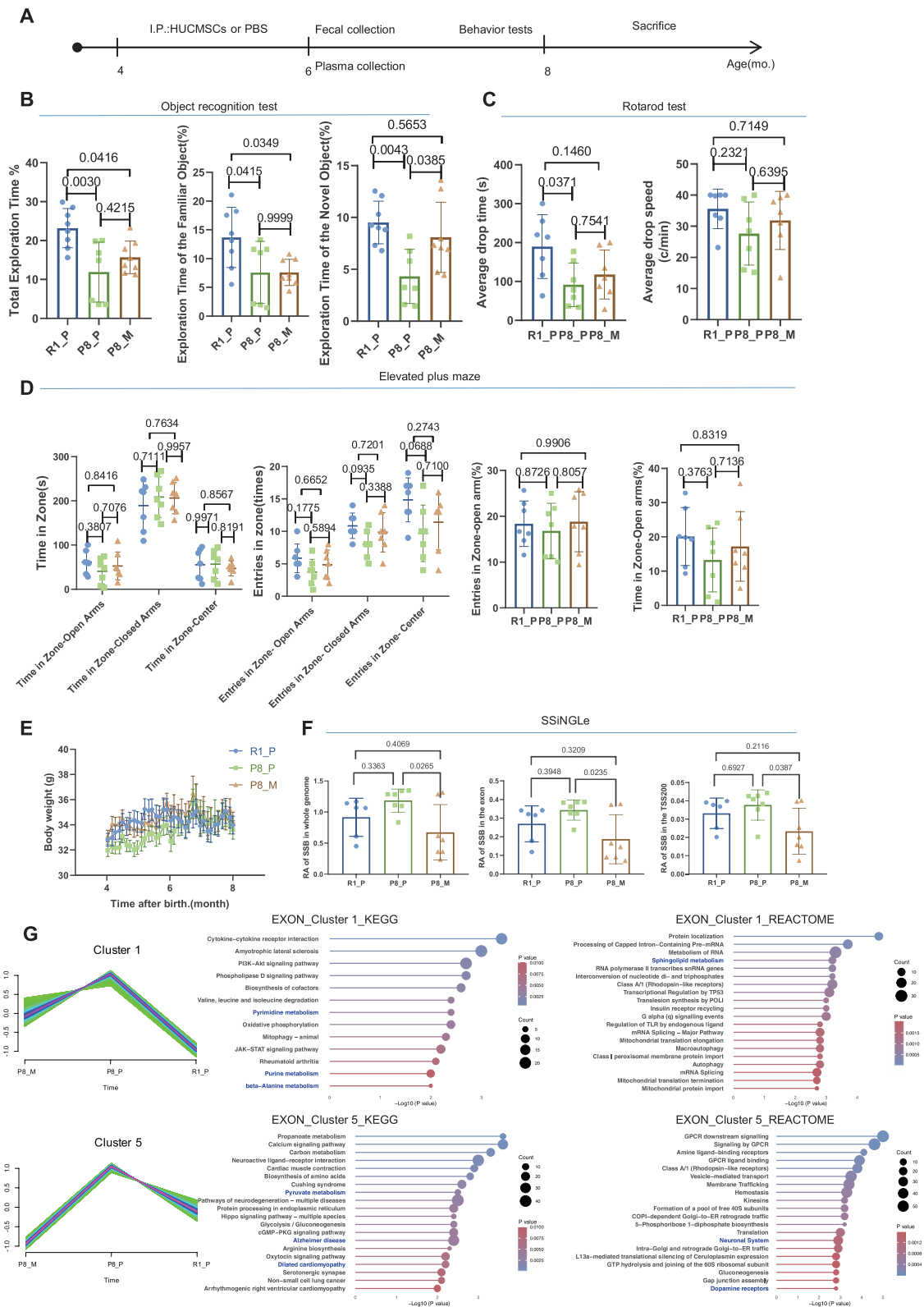


Fig. 1 (See legend on previous page.)

Trend analysis of relative DNA strand break (SSB) abundance in exon regions across the three groups was performed using the mfuzz R package. Functional enrichment analysis for each gene cluster was conducted through Metascape (<https://metascape.org>).

16S rRNA sequencing and data analysis

Microbiome DNA extraction

DNA was extracted using MagPure Stool DNA LQ Kit (Magen Biotechnology Co., Ltd., China). Five 96-well deep plates were prepared by adding 600 μ L of Buffer with magnetic beads, 20 μ L of Proteinase K, 5 μ L of RNase A, and 700 μ L of each wash buffer (Wash 1: Buffer GW1, wash 2: 75% ethanol, wash 3: 75% ethanol). Additionally, 100 μ L of Elution Buffer was added to each well. Samples weighing 100–200 mg were placed into centrifuge tubes containing grinding beads and 1 mL of Buffer ATL/PVP-10. The samples were ground and subsequently incubated at 65°C for 20 min. After centrifugation at 14,000 \times g for 5 min, the supernatant was transferred to a new tube, to which 0.6 mL of Buffer PCI was added, and the mixture was vortexed for 15 s. The tubes were then centrifuged at 18,213 \times g for 10 min. The resulting supernatant was transferred to a deep well plate prepped with magnetic beads binding solution. The plates were positioned in a designated section of the Kingfisher machine and processed according to the programmed settings. Finally, the DNA was transferred to 1.5 mL centrifuge tubes.

Meta amplicon library preparation and sequencing (DNBSEQ platform of MGI)

Amplicon metagenomic sequencing targeted variable regions of bacterial 16S rDNA, facilitating analysis of microbial community diversity. The process involved the use of sequencing and fusion primers for amplifying these regions, followed by high-throughput sequencing on the DNBSEQ platform. Quality control (QC) was performed on the samples using appropriate methods. Specific quantities of genomic DNA were extracted, and a fusion primer reaction system was prepared for PCR amplification. Library QC was conducted using necessary testing techniques. Single-stranded PCR products were produced, set for circularization reaction, and uncyclized linear DNA molecules were digested. Single-stranded circular DNA was replicated via rolling cycle amplification to form DNA nanoballs, which were loaded onto patterned nanoarrays for sequencing using combinatorial probe-anchor synthesis (cPAS).

Meta amplicon analysis method

Data filtering generated high-quality clean reads by truncating low-quality sequences and removing reads contaminated with adapters or containing ambiguous bases [7].

DATA2 was utilized to generate amplified sequence variants (ASVs) by 100% similarity denoising sequences. ASV taxonomy annotation was performed by aligning ASV representative sequences for taxonomic annotation using the SILVA classifier (V138 2019-12-16), filtering out irrelevant annotations. Alpha diversity was analyzed using mothur, and beta diversity was examined through QIIME software to explore species complexity across samples [8–12]. Predictive functional profiling of microbial communities was conducted using PICRUSt2 (v2.2.0-b), R (v3.4.10) based on gene sequencing profiles, which provided enhanced accuracy and a broader database compared to its predecessor [13]. The Wilcoxon test was applied to compare the difference functions between the two groups of sample. In the Results section, we followed industry practice and referred to ASVs (Amplicon Sequence Variants) as OTUs (Operational Taxonomic Units).

Metabolites quantitative analysis

Hemolysis in some samples resulted in sample culling without metabolite analysis result in 11 samples per group.

Sample preparation and carboxyls labeling

Plasma samples were thawed, vortexed, and then aliquoted into 1.5 mL centrifuge tubes, with each sample divided into six portions for multi-channel analysis (30 μ L/channel). For pooled sample preparation, 75 μ L of serum from each sample was combined, vortexed to ensure thorough mixing, and labeled as a reference sample. To precipitate proteins, 90 μ L of pre-chilled mass spectrometer-grade methanol was added to each sample. Samples were vortexed, centrifuged at 12,000 rpm for 10 min at 4°C, and the supernatants were transferred to new tubes and dried under nitrogen. Samples designated for carboxyl submetabolome analysis were treated with 25 μ L of a 3:1 v/v acetonitrile/water solution. 10 μ L of reaction catalytic reagent and 25 μ L of carbon-12 or carbon-13 labeled reagents were added, followed by incubation at 80°C for 60 min. Post-incubation, 40 μ L of quenching reagent was added and the mixture was further incubated for 30 min at the same temperature.

Ultra-high-performance liquid chromatography-quadrupole-time of flight/mass spectrometry (UHPLC-Q-TOF/MS)

Chromatographic separation was performed using an Agilent Eclipse Plus reversed-phase C18 column (150×2.1 mm, 1.8 μm) on an Agilent 1290 Liquid Chromatograph, linked to an Agilent 6546 Q-TOF Mass Spectrometer (Agilent Technologies, USA). The mobile phases used were 0.1% formic acid in water (A) and 0.1% formic acid in acetonitrile (B). The gradient program started with 25% B, ramping to 99% B over 10 min and held for 5 min, before returning to 25% B at 15.1 min and held until 18 min. The column temperature was maintained at 40°C, and the flow rate was set at 400 μL/min. The ion source parameters were set as follows: Gas Temp: 325°C; Dry Gas: 8 L/min; Nebulizer: 35 psi; Sheath Gas Temp: 400°C; Sheath Gas Flow: 12 L/min; MS scanning range: m/z 220–1000.

Data analysis

Data were processed using IsoMS Pro 1.2.16. Metabolites present in at least 80% of the samples in one group were retained. Structural identification of metabolites utilized a three-tier system, and differential metabolites were identified based on fold changes and FDR-corrected *p*-values using statistical thresholds of fold change greater than 1.2 or less than 0.83 and a *p*-value less than 0.05. Pathway analysis was conducted using MetaboAnalyst, employing Global Test and Relative-betweenness Centrality for enrichment and topology analysis, respectively. *Mus musculus* (KEGG) was used for analysis.

Microbiota and metabolites combinational analysis

Data from stool-plasma paired samples were used to perform microbiota and metabolites combinational analysis, and SPEARMAN correlation coefficients and *p*-values were calculated by R(v3.4.10).

Statistical analysis

Data was analyzed using R packages unless otherwise indicated. The specific statistical analysis methods were all specified in the legends otherwise in the related experimental methods. Besides, to check if the data was normally distributed, we used graphical methods like Q-Q plots or statistical tests like the Shapiro–Wilk test. If the data does not meet the normality assumption, we applied non-parametric tests like the Mann–Whitney U test or Kruskal–Wallis test instead of parametric tests. If the assumption of homogeneity of variances was violated with outlier, we used Welch's ANOVA instead of the standard ANOVA, which does not assume equal variances, and mixed-effects models were used to account for dependencies.

Results

Enhancement of behavioral and physical functions by clinical-grade HUCMSCs in SAMP8 mice

Clinical-grade HUCMSCs were prepared, and quality tests including morphology, phenotype, and differentiation potential were performed (Figure S1). Two months post-transplantation, the mice underwent a series of behavioral tests including object recognition, rotarod, elevated plus maze, and Morris water maze for evaluating spatial learning and memory (Fig. 1A). Notably, the object recognition results indicated a significant increase in curiosity among the SAMP8 mice compared to the control groups. Tukey's multiple comparison test following a one-way ANOVA confirmed significant differences in "Exploration Time of the Novel Object." The test identified a decrease in exploration time in the SAMP8_PBS group compared to the SAMR1_PBS group ($p=0.0043$), and an increase in exploration time in the SAMP8_MSC group compared to the SAMP8_PBS group ($p=0.0385$). These findings highlight the enhanced curiosity in the SAMP8_MSC mice. (Fig. 1B, Table S1). The rotarod test revealed improved motor coordination and balance in SAMP8 mice treated with MSCs compared to controls, as evidenced by increased drop times (Fig. 1C, Table S2). The elevated plus maze results suggested reduced anxiety levels, with MSC-treated mice showing increased explorations of open arms (Fig. 1D, Table S3). Furthermore, MSC treatment counteracted the underweight phenotype typically observed in SAMP8 mice (Fig. 1E, Table S4). However, no significant differences were noted in the water maze tests among the groups (data not shown).

Genome-wide analysis reveals MSC treatment reduces DNA single-strand breaks in aging mice

To further investigate the role of MSCs in aging, we conducted a genome-wide analysis of DNA single-strand breaks called SSiNGLe, focusing on their distribution across the entire genome, exonic regions, and within 200 bp of transcription start sites (TSS). Using the SSiNGLe technique, we found that SSB levels in the SAMP8_PBS group were higher than those in the SAMR1_PBS group ($p=0.3363$, $p=0.3948$, $p=0.6927$ for genome-wide, exon regions, and within 200 bp of TSS, respectively). In the MSC-treated SAMP8_MSC group, SSB levels were significantly reduced across the genome compared to the SAMP8_PBS group ($p=0.0265$, $p=0.0235$, $p=0.0387$ for genome-wide, exon regions, and within 200 bp of TSS, respectively), while there were no significant differences between the SAMR1_PBS and SAMP8_MSC groups ($p=0.4069$, $p=0.3209$, $p=0.2116$ for genome-wide, exonic regions, and within 200 bp of TSS, respectively) (Fig. 1F, Table S5). These results suggest

that MSC treatment may alleviate age-related molecular pathologies by reducing DNA damage in critical genomic regions, further supporting the potential role of MSCs in anti-aging therapy.

Trend analysis of relative SSBs abundance in exon regions across the three groups was conducted using the *mfuzz* R package. Certain gene clusters exhibited higher SSB abundance in the SAMP8_PBS group compared to the SAMR1_PBS group, with a subsequent reduction in DNA strand breaks in the SAMP8_MSC group relative to the SAMP8_PBS group. The pathways annotated for these genes include those associated with immune and metabolic processes in Exon_cluster 1, which were linked to several Reactome and KEGG pathways. Additionally, genes within Exon_cluster 5 were associated with pathways related to GPCR, the neuronal system, and dopamine receptors, aligning with the known regulatory effects of mesenchymal stem cells (MSCs) on anxiety levels (Fig. 1G, Table S6). These findings suggest the need for a comprehensive metabolic analysis in the model mice to further explore the underlying mechanisms.

Pathological improvements in organ tissues of SAMP8 mice following MSC treatment

Histopathological evaluations of various tissues including the brain, heart, lung, skeletal muscle, liver, spleen, kidney, and colon revealed significant improvements in MSC-treated mice (Fig. 2). In the brain, the frontal lobe and hippocampal regions of treated mice maintained structural integrity and normal glial cell distribution, contrasting with the compact and stressed neuronal arrangements seen in untreated mice. This preservation suggests enhanced neuronal resilience and protein synthesis, as indicated by stable NISSL body counts during active phases [14]. Grayscale value analysis of Nissl staining revealed that the hippocampal region in the SAMP8_PBS group exhibited lighter staining compared to the SAMR1_PBS group ($p=0.0002$). Following MSC treatment, the SAMP8_MSC group showed significant improvement in staining intensity relative

to the SAMP8_PBS group ($p=0.0012$), with no significant difference observed between the SAMP8_MSC and SAMR1_PBS groups ($p=0.7538$) (Fig. 2A–H, Table S7). Cardiac assessments demonstrated normal myocardial fiber arrangement in MSC-treated SAMP8_MSC mice, resembling the healthy cardiac tissues of the SAMR1_PBS group and contrasting with the mild edema and fibrosis observed in the SAMP8_PBS controls. Additionally, statistical analysis of the minimum ventricular wall thickness showed that the SAMP8_PBS group had a thinner ventricular wall compared to the SAMR1_PBS group ($p=0.0029$). The SAMP8_MSC group exhibited significant improvement following MSC treatment compared to the SAMP8_PBS group ($p=0.0007$), with no significant difference observed between the SAMP8_MSC and SAMR1_PBS groups ($p=0.8796$), suggesting that MSCs ameliorated the dilated cardiomyopathy phenotype (Fig. 2I–L, Table S7). In the gastrointestinal tract, villous structures and epithelial cell arrangements remained well-preserved in treated mice, indicating reduced degenerative changes. Lung evaluations showed reduced inflammation and preserved architecture in MSC-treated groups compared to controls, which displayed disorganized tissue and significant inflammation (Figure S2A–C).

In the kidneys, SAMP8_MSC mice exhibited well-preserved structures with clear corticomedullary differentiation and intact glomeruli. The SAMP8_PBS group showed signs of early renal stress with tubular dilation and mild vacuolization, whereas R1 mice displayed more pronounced chronic alterations such as fibrosis and tubular atrophy (Figure S2A–C). The muscle tissue analysis highlighted that SAMP8_MSC mice had regularly arranged muscle fibers, consistent nuclear placement, and no signs of damage. In contrast, the SAMP8_PBS group exhibited slight loosening of fiber spacing suggestive of mild edema, and the R1 group showed signs of tissue degeneration with increased spacing and irregular fiber cross-sections (Figure S2A–C). Spleen analysis supported the resilience of SAMP8_MSC mice with clear demarcations between white and red pulp, unlike the

(See figure on next page.)

Fig. 2 Representative histopathological images of the brain coronal sections and the heart four-chamber sections. **A–C** HE staining and Nissl staining results of the frontal lobe in different groups. **D** Statistical analysis of Nissl staining in the frontal lobe (The statistical method involves converting positive staining into grayscale, calculating the grayscale value and area, and determining the Nissl staining quantification result for each sample by dividing the grayscale value by the area, using Python 3.7). **E–G** HE staining and Nissl staining results of the hippocampus in different groups. **H** Statistical analysis of Nissl staining in the hippocampus (The statistical method involves converting positive staining into grayscale, calculating the grayscale value and area, and determining the Nissl staining quantification result for each sample by dividing the grayscale value by the area, using Python 3.7). **I–K** Cross-sectional HE-stained images of heart tissue. HE staining of heart tissue with red arrows in J-2 indicating disorganized sarcomeres in the myocardium of SAMP8 mice. **L** Statistical analysis of the minimum ventricular wall thickness measured on panoramic scanned images of HE-stained sections using Qupath software. $n=7\sim 8$ per group. The pathology images in the figure were representative images of animals euthanized on the 78th day after the first HUCMSCs injection. Data were analyzed using one-way ANOVA followed by Tukey's post-hoc test in subfigure D, H, L. *Abbreviation:* R1_P: SAMR1_PBS; P8_P: SAMP8_PBS; and P8_M: SAMP8_MSC

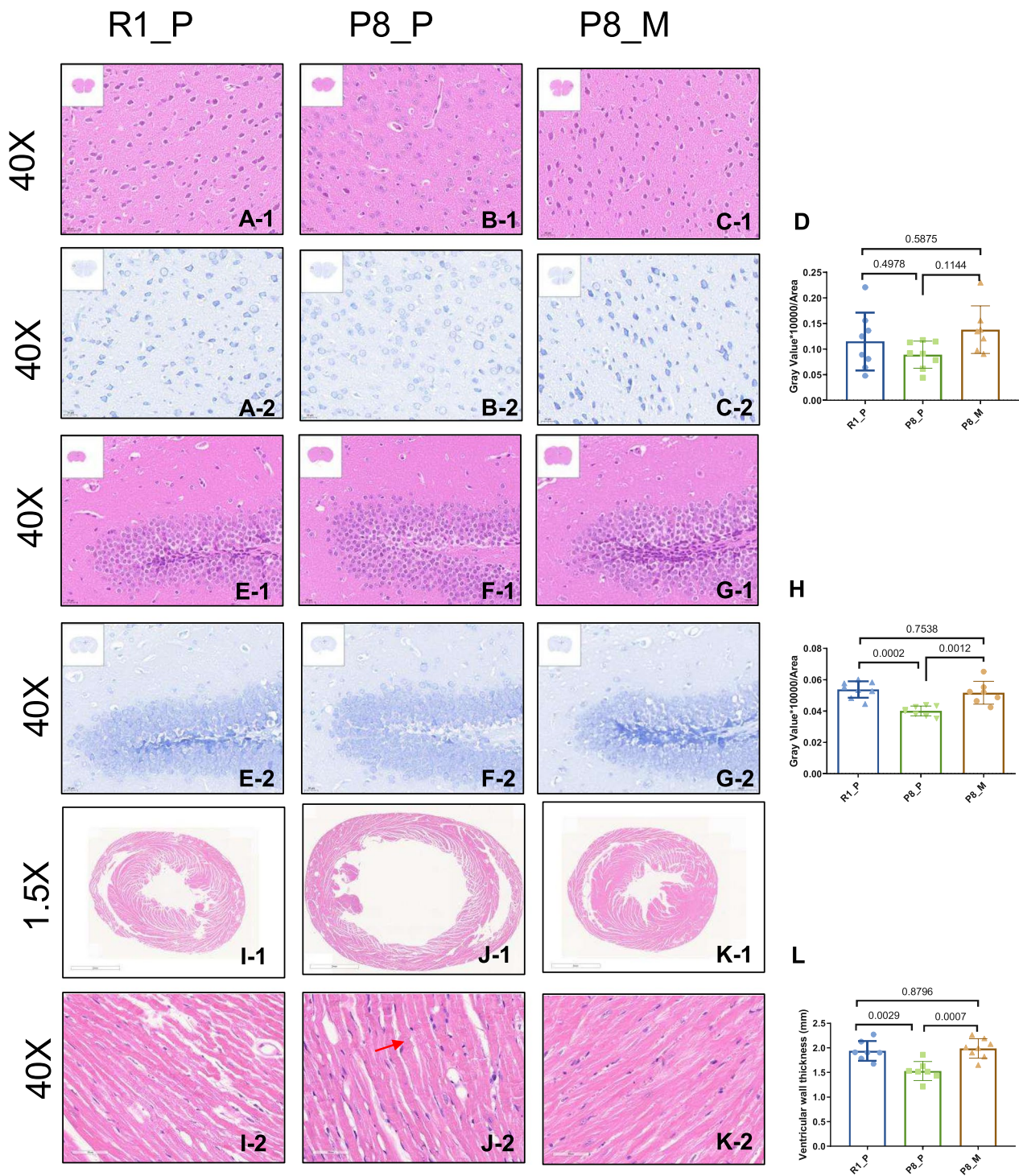


Fig. 2 (See legend on previous page.)

more severe structural disruptions and inflammation observed in R1 mice (Figure S2A-C).

Lastly, liver tissues across all groups displayed minimal changes, suggesting overall healthy organ condition (Figure S2A-C).

Overall, the SAMP8_MSC group, treated with mesenchymal stem cells (MSCs), exhibited superior tissue preservation and minimal pathological changes compared to the SAMP8_PBS group, and in some tissues, such as kidneys, muscles and spleen, even surpassed the R1 control

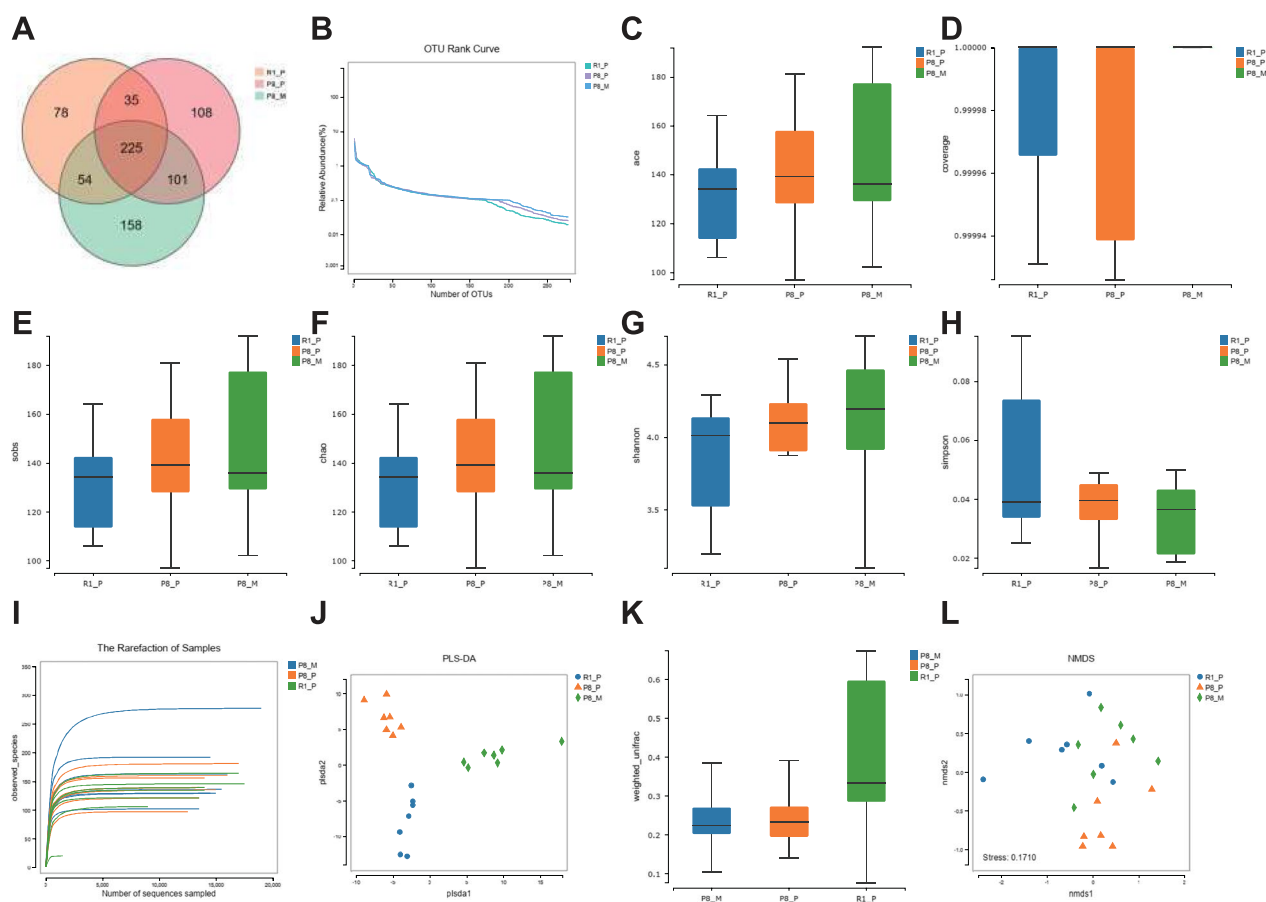


Fig. 3 Fecal microbial diversities were assessed among three experimental groups: SAMR1_PBS group, SAMP8_PBS group, and SAMP8_MSC group. Fecal pellets were collected one week after the final MSC injection, and 16S rRNA sequencing was performed following the protocol outlined in the methods section. Alpha_diversity and beta_diversity analyses were conducted across the three groups ($n=7$ per group). **A** Venn diagram illustrating the shared and unique operational taxonomic units (OTUs) among multiple samples, providing insights into OTU overlap across samples and identifying core microbial species associated with different environments. Different colored shapes represent distinct samples or groups, with overlapping numbers indicating shared OTUs between two samples or groups. Likewise, multiple overlapping numbers indicate shared OTUs among multiple samples or groups. Analysis performed using the VennDiagram package in R (v3.1.1). **B** OTU Rank curve depicting species diversity within samples, assessing both richness and evenness of species abundance. Each OTU's relative abundance in each sample was calculated and arranged in descending order of abundance, with OTU rank on the x-axis and relative abundance on the y-axis. Analysis performed using R (v3.1.1). **C–H** Box plots illustrating inter-group alpha diversity differences. Kruskal-Wallis test was used for comparisons among three or more groups. P values were noted ($p=0.5964$ for sobs, $p=0.5964$ for chao $p=0.5788$ for ace, $p=0.4788$ for shannon, $p=0.5680$ for coverage, $p=0.6478$ for simpson) for various alpha diversity metrics. Analysis performed using R (v3.2.1) and the ggplot package in R (v3.4.1). **I** Dilution curve plotting alpha diversity metrics against sequencing depth, providing insights into sequencing depth sufficiency. Analysis conducted using R (v3.1.1). **J** Partial least squares discriminant analysis (PLS-DA) depicting group-wise discrimination. Different colored or shaped points represent samples under different conditions or environments. Axes represent relative distances, and their interpretation requires consideration of sample characteristics. Analysis performed using the mixOmics package in R (v3.2.1). **K** Box plots visualizing inter-group differences in beta diversity, with statistical significance indicated ($p=0.0025$). Analysis conducted using the ggplot package in R (v3.4.1). **L** Non-metric multidimensional scaling (NMDS) plot assessing community dissimilarities. Anosim analysis was performed to evaluate group-wise differences. Stress values were provided to assess NMDS quality. $p=0.0065$, $R=0.1834$. Analysis conducted using the vegan package in R

group. This demonstrates that MSC treatment not only mitigates age-related degenerative changes but may also rejuvenate certain tissues, offering promising implications for regenerative medicine.

Alterations in intestinal flora as indicated by fecal 16S rDNA sequencing in the senescence accelerated mouse model

Fecal 16S rDNA sequencing highlighted significant changes in the intestinal flora induced by MSC treatment. Venn diagram analysis showed overlapping operational taxonomic units (OTUs) among the SAMR1_PBS,

SAMP8_PBS, and SAMP8_MSC groups, illustrating shared microbial species (Fig. 3A). The OTU Rank curve, representing species richness and evenness, depicted similar distributions across the groups (Fig. 3B).

Diversity indices such as Sobs, Ace, Chao, and Shannon showed no significant differences among the groups ($p > 0.05$), indicating stable microbial diversity post-treatment (Fig. 3C–G). Meanwhile, the Simpson diversity index was marginally lower in the SAMP8_MSC group compared to the SAMR1_PBS and SAMP8_PBS groups ($p = 0.38287$ and $p = 0.62005$, respectively), indicating higher microbial diversity in the SAMP8_MSC group relative to the other two groups (Fig. 3H). Rarefaction analysis suggested a higher microbial richness in the SAMR1_PBS group compared to the SAMP8_PBS group, with SAMR1_PBS samples typically achieving saturation at 102–270 OTUs versus 97–181 OTUs for SAMP8_PBS (Fig. 3I, Table S8). A Partial Least Squares Discriminant Analysis (PLS-DA) plot based on weighted UniFrac distances ($p = 0.0025$) revealed distinct microbial clustering for each group, indicating differentiated community structures (Fig. 3J, K). The Analysis of Similarities (ANOSIM) supported these findings, showing significant differences in microbiota composition between the groups ($p = 0.0065$, $R = 0.1835$, $\text{Stress} = 0.1710$) (Fig. 3L). These results collectively demonstrate distinct variations in gut microbiota across the groups, influenced by MSC treatment.

Comparative analysis of gut microbiota across different groups

Species histograms were constructed to display the composition and relative proportions of each sample, highlighting variations in microbial populations (Fig. 4A–B, Table S9). This analysis classified species by their abundance at the genus level, with the top 10 most abundant species depicted in the histograms (Fig. 4C). Notably,

species considered beneficial "probiotics" in humans, such as *Prevotellaceae*, *Lachnospiraceae_AC2044* and *Roseburia*, were significantly restored in the MSC-treated SAMP8_MSC group compared to the SAMP8_PBS group (Fig. 4D–F).

Further, LEfSe clustering analysis identified specific microbial taxa such as *Eubacterium coprostanoligenes*, *Butyricococcus*, *Butyricoccaceae*, *Desulfovibrio* as significantly influencing the microbial communities of the SAMR1_PBS or SAMP8_MSC groups (Fig. 5A–F). *Eubacterium coprostanoligenes* is noted for its cholesterol-reducing capabilities, suggesting health benefits that may translate to humans [15]. *Butyricococcus* and related strains from the *Butyricoccaceae* family have been effective in maintaining gut flora balance and mitigating gastrointestinal conditions [16,17]. Interestingly, *Desulfovibrio*, despite its potential negative impacts, has demonstrated neutral or beneficial roles under specific conditions [18], the dynamic nature of gut microbial interactions. The functional predictions and enrichment analyses suggested that the key differences between groups primarily involve metabolic pathways such as primary bile acid biosynthesis, fatty acid degradation, and N-Glycan biosynthesis (Table S10–S12).

Metabolic regulation by MSC administration

Previous research indicates that decreased levels of probiotics may contribute to coronary artery disease and heart failure by reducing inflammation through SCFA synthesis [19]. To explore the metabolic changes following MSC administration, we conducted a comprehensive non-targeted metabolomics analysis (Table S13). This revealed significant alterations in several key metabolites. For instance, levels of 2-Aminomuconic acid, isomer 2 of 1-Pyrroline-2-carboxylic acid, Pelargonic Acid, Traumatic acid, Methionyl-Valine were notably lower in the SAMP8-MSC group compared to the SAMR1-PBS or

(See figure on next page.)

Fig. 4 Structural comparison of the fecal microbiota among the SAMR1_PBS group, SAMP8_PBS group, and SAMP8_MSC group ($n = 7$ per group).

A, B Taxonomic bar plots illustrating the composition and proportions of species in each sample, reflecting inter-sample species variations. OTUs were taxonomically classified by comparison with databases, and species abundance bar plots were generated at the genus level for each sample (species with average abundance below 0.5% and those unannotated at the specified taxonomic level were merged into "Others"). Sample names are plotted on the x-axis, while relative species abundance is depicted on the y-axis. Analysis conducted using R (v3.4.1). **C** Differential comparison of key species at the genus level. The top 10 abundant species were selected to display the average relative abundance in each group and the significance of differences ($p < 0.001$ denoted as "****"; $0.001 < p < 0.01$ denoted as "***"; $0.01 < p < 0.05$ denoted as "**"; no notation if $p > 0.05$). Analysis conducted using R (v3.4.1). **D–F** Differential analysis of species at the genus level: **D** *Prevotellaceae_UCG_001*, **E** *Lachnospiraceae_AC2044*, **F** *Roseburia*. Wilcoxon Test results of species differential analysis: Left panels display the relative abundance bar plots of each group; the middle panels show the \log_2 -transformed average relative abundance ratio of the same species between the two groups; the right panels present the p -value and FDR values obtained from the Wilcoxon test. If both p -value and FDR values are less than 0.05, significant differences exist between the two groups. The Wilcoxon rank-sum test, also known as the Mann-Whitney U test, is a non-parametric method for comparing independent samples. By examining the average ranks of the two sample groups, Wilcoxon rank-sum test analysis can identify significant differences in species between the two groups and calculate FDR values for p -value adjustment. Kruskal-Wallis test analysis can identify species with significant differences ($p < 0.05$) among different groups. Analysis conducted using R (v3.4.1).

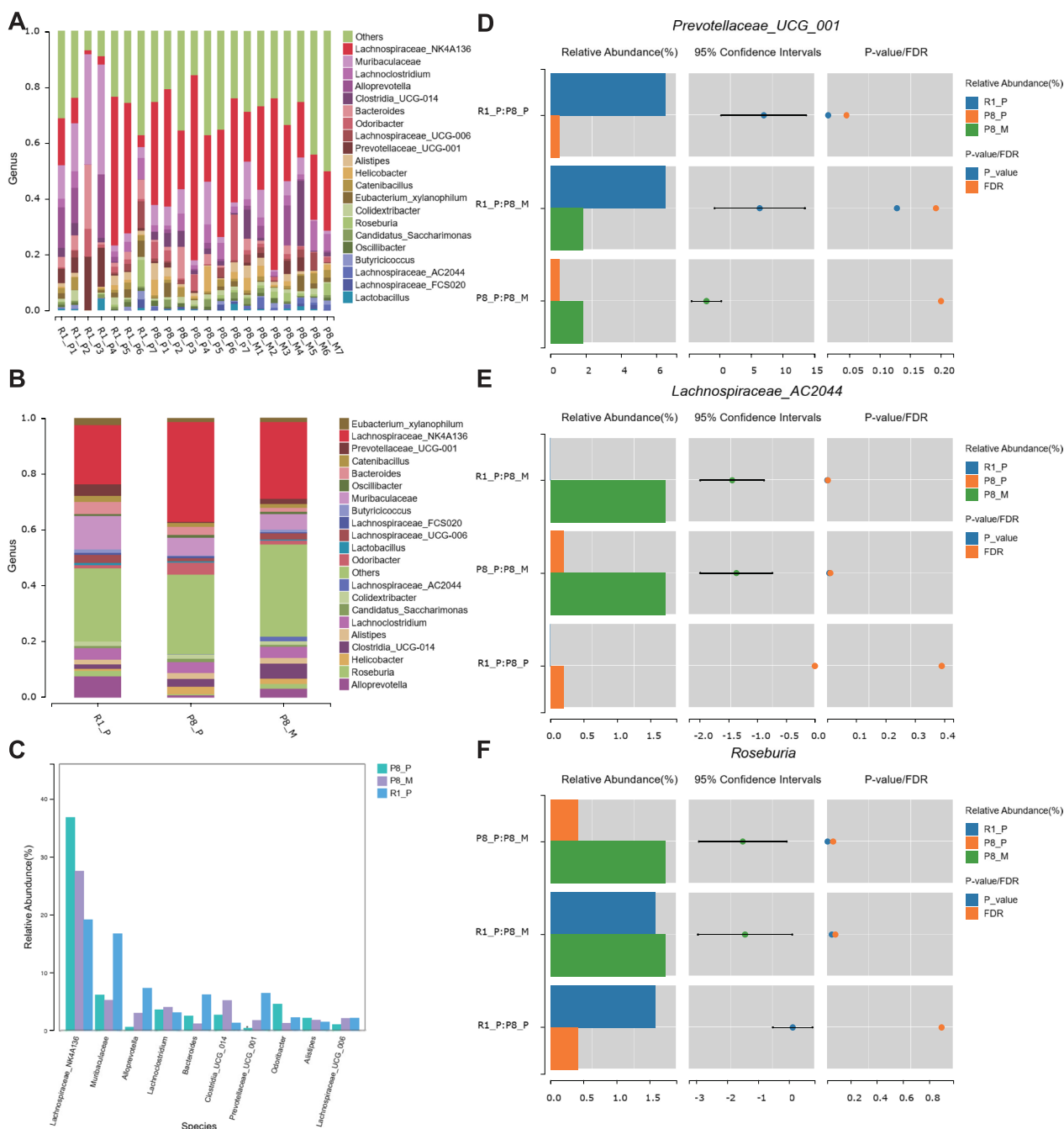


Fig. 4 (See legend on previous page.)

SAMP8-PBS groups, suggesting that MSCs may modulate these metabolites to exert their effects (Fig. 6A–E). Furthermore, MSC administration led to increased levels of metabolites beneficial for cardiovascular health, including 4-Hydroxyphenylacetic acid (4-HPAA), Dodecanoic acid, 2-Benzylsuccinic acid, 5-dodecenoic acid and 3-methyl-Histidine (Fig. 6F–J). Additionally, elevated levels of 5-Hydroxy-L-tryptophan in the SAMP8_MSC

group compared to the SAMP8_PBS group (Fig. 6K) suggest potential normalization of serotonin synthesis [20], which is linked to antidepressant properties and observed reductions in depression-like behaviors in animals (Fig. 2).

Complex interactions and effects of metabolites

Certain metabolites exhibit effects that align or conflict with established benefits or harms, depending on their specific roles within metabolic pathways and concentrations in the body. Notably, excessive levels of some metabolites can be linked to health issues such as neurological damage from abnormalities in amino acid metabolism. For instance, MSC administration restored levels of Octadecanedioic acid which when elevated in pregnant women, is associated with an increased risk of gestational diabetes mellitus [21] (Fig. 6L). N-Acetyl-DL-serine, typically a uremic toxin at high levels [22, 23], showed elevated levels in the SAMP8-PBS/MSc group compared to the SAMR1 group, suggesting its beneficial role under controlled conditions (Fig. 6M), indicating it may play a vital role under controlled levels. Vanillic acid, known for its geroprotective properties in *Caenorhabditis elegans* [24] was higher in the SAMR1-PBS group than in the SAMP8 groups, with MSC treatment not altering this trend, indicating limitations in MSC's therapeutic scope regarding certain metabolites (Fig. 6N).

However, saccharopine, involved in lysine catabolism and implicated in mitochondrial disruption [25], was increased in the SAMP8-MSc group, underscoring the complex effects of MSCs on metabolic pathways (Fig. 6O). Interestingly, levels of **N-acetyl-Ornithine**, not previously reported to change in diseases [26] or aging, were elevated in the SAMP8-MSc group, suggesting novel roles for this metabolite in response to MSC treatment (Fig. 6P).

Furthermore, the enrichment analysis of differential metabolite pathways indicated significant differences among the groups in pathways related to fatty acid and

amino acid metabolism, highlighting the profound impact of MSC therapy on metabolic functions (Figs. 6Q-S, Table S14-S16).

Correlations between gut microbiota and metabolite profiles

Further analysis explored the correlation between gut microbiomes and metabolites, uncovering specific roles of various microbiomes in influencing metabolite dynamics (Fig. 7, Table S17-S19). Some metabolite biomarkers previously reported to decline during aging are positively correlated with potentially beneficial bacteria. For example, in the SAMP8_PBS vs SAMP8_MSc comparison groups, significant differences in fecal microbiomes and metabolites, such as 5-dodecenoic acid is positively correlated with *Eubacterium_xylanophilum* and *Lactobacillus*. In the SAMR1_PBS vs SAMP8_PBS comparison groups, 4-Hydroxyphenylacetic acid is positively correlated with *Desulfovibrio* and *Lachnospiraceae_UCG-006*; Vanillic Acid is positively correlated with *Colidextribacter*; Dodecanoic acid is positively correlated with *Prevotellaceae_UCG-001*, *Butyricoccus*, and *Lachnospiraceae_UCG-006*. Among the three comparison groups, 4-Hydroxyphenylacetic acid is significantly positively correlated with *Intestinimonas*, *Roseburia*, *Eubacterium_xylanophilum*, and *Lachnospiraceae_FCS020*. Some metabolite biomarkers previously reported to decline during aging or pathological states are negatively correlated with potentially harmful bacteria. For example, in the SAMP8_PBS vs SAMP8_MSc comparison groups, 4-Hydroxyphenylacetic acid is negatively correlated with *Marvinbryantia*, *Rikenella*, and *Helicobacter*. In the SAMR1_PBS vs SAMP8_PBS comparison

(See figure on next page.)

Fig. 5 Dominant microorganisms among the SAMR1_PBS group, SAMP8_PBS group, and SAMP8_MSc group ($n=7$ per group). **A, C, E** LEfSe clustering trees comparing differential species between SAMR1_PBS and SAMP8_PBS (**A**), SAMP8_PBS and SAMP8_MSc (**C**), and SAMR1_PBS and SAMP8_MSc (**E**) groups pairwise. As depicted in LEfSe clustering tree, different colors represent different groups, with color_coded nodes indicating microbial taxa that play a significant role within each group. Each colored dot represents a biomarker, with biomarker names provided in the legend at the bottom right corner. Yellow nodes denote microbial taxa that do not play a significant role across different groups. Taxonomic levels from inner to outer circles include phylum, class, order, family, and genus. LEfSe is a software used for discovering high-dimensional biomarkers and revealing genomic features. It encompasses genes, metabolism, and taxonomy to discriminate between two or more biological conditions (or groups), emphasizing statistical significance and biological relevance, enabling researchers to identify differentiating features and associated taxonomic categories. It employs biological statistical differences for robust identification and conducts additional tests to assess whether these differences conform to expected biological behavior. Software used: LEfSe (<https://huttenhower.sph.harvard.edu/galaxy/>). **B, D, F** LDA plots comparing differential species between SAMR1_PBS and SAMP8_PBS (**B**), SAMP8_PBS and SAMP8_MSc (**D**), and SAMR1_PBS and SAMP8_MSc (**F**) groups pairwise, displaying LDA scores corresponding to species with $p < 0.05$. LDA plots illustrating significant microbial taxa within different groups. Colors represent microbial taxa significantly influencing different groups. The plot primarily displays biomarkers with LDA scores greater than the preset value (2.0). The color of the bars represents the respective groups, while the length represents the LDA score, indicating the magnitude of the significant differences between groups. LDA is a classic and popular algorithm in the field of machine learning and data mining, serving as a supervised dimensionality reduction technique, where each sample in the dataset has a categorical output. This differs from PCA, which is an unsupervised dimensionality reduction technique that does not consider sample category outputs. Compared to PCA analysis, LDA algorithm effectively utilizes sample grouping information, resulting in more reliable outcomes. Software used: LEfSe (<https://huttenhower.sph.harvard.edu/galaxy/>)

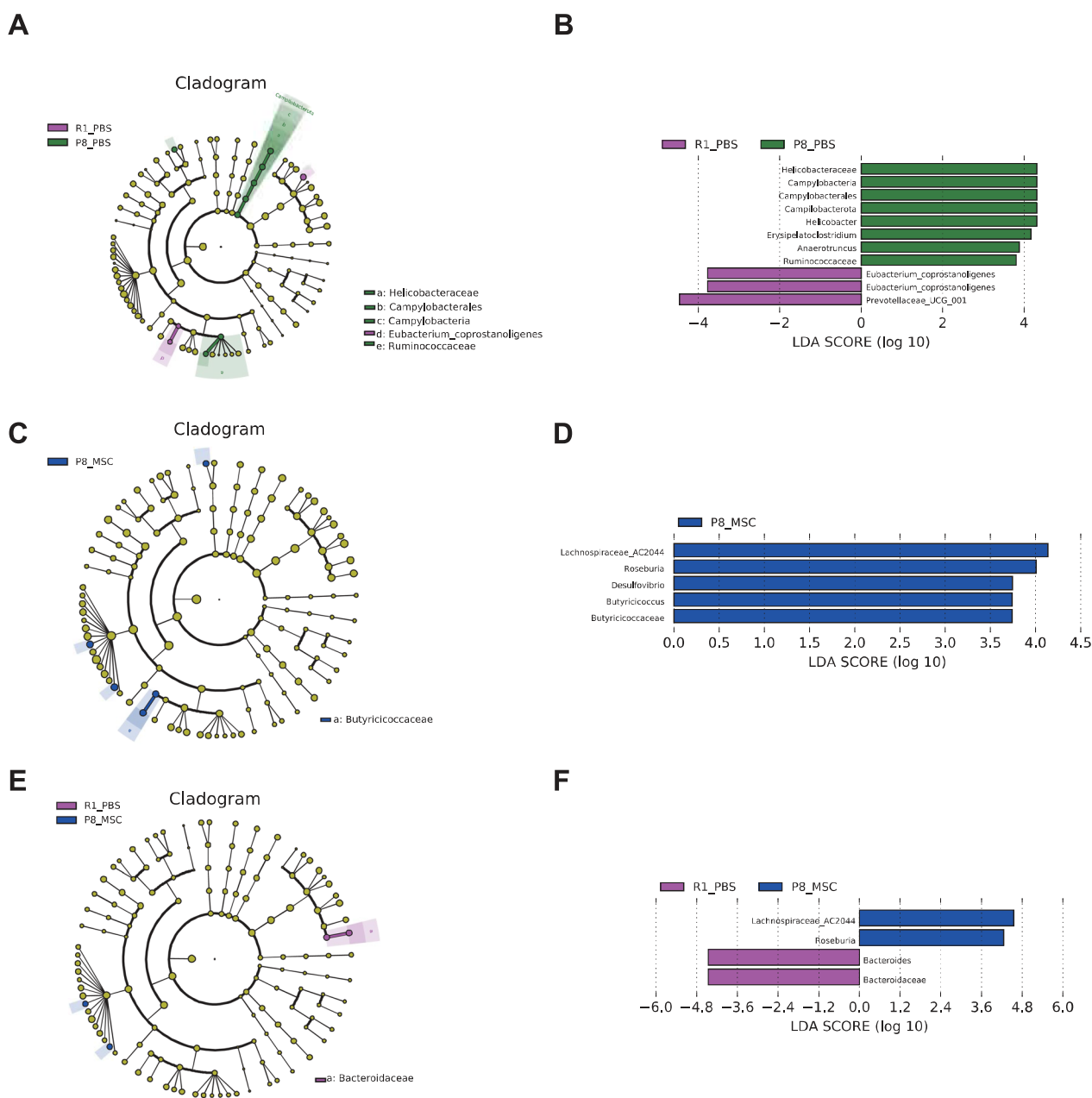


Fig. 5 (See legend on previous page.)

(See figure on next page.)

Fig. 6 Metabolic characteristics of SAM Mice. These violin plots illustrates the levels of metabolites within the Identification Level categories Tier 1 and Tier 2 across three groups or specifically between SAMP8_PBS and SAMP8_MSC. Each subfigure is labeled with the corresponding metabolite and statistical values (F value and *p* value) above it. For subfigures **A-I** and **L-P**, each group consists of 11 samples (*n* = 11). For subfigures **J-K**, one outlier sample with aberrant coloration caused by jaundice was excluded from the SAMP8_MSC group, reducing its sample size to 10 (*n* = 10), while the other two groups remain unchanged at 11 samples each (*n* = 11). *P* values between groups were calculated using Welch's *t*-test; *P* values among three groups were calculated using one-way ANOVA. *Q* value equals FDR-adjusted *p*-value (Storey's *q*-value). Bubble charts illustrating pathway analysis differences between: **(Q)** SAMP8_MSC and SAMP8_PBS groups, **(R)** SAMP8_MSC and SAMR1_PBS groups, **(S)** SAMP8_PBS and SAMR1_PBS groups. The x-axis represents the impact score of metabolic pathways, while the y-axis shows significance levels calculated via enrichment analysis. Each bubble represents a distinct metabolic pathway; the size of the bubble indicates the impact score of the pathway, and the shade of the bubble color denotes the statistical significance of the metabolic pathways

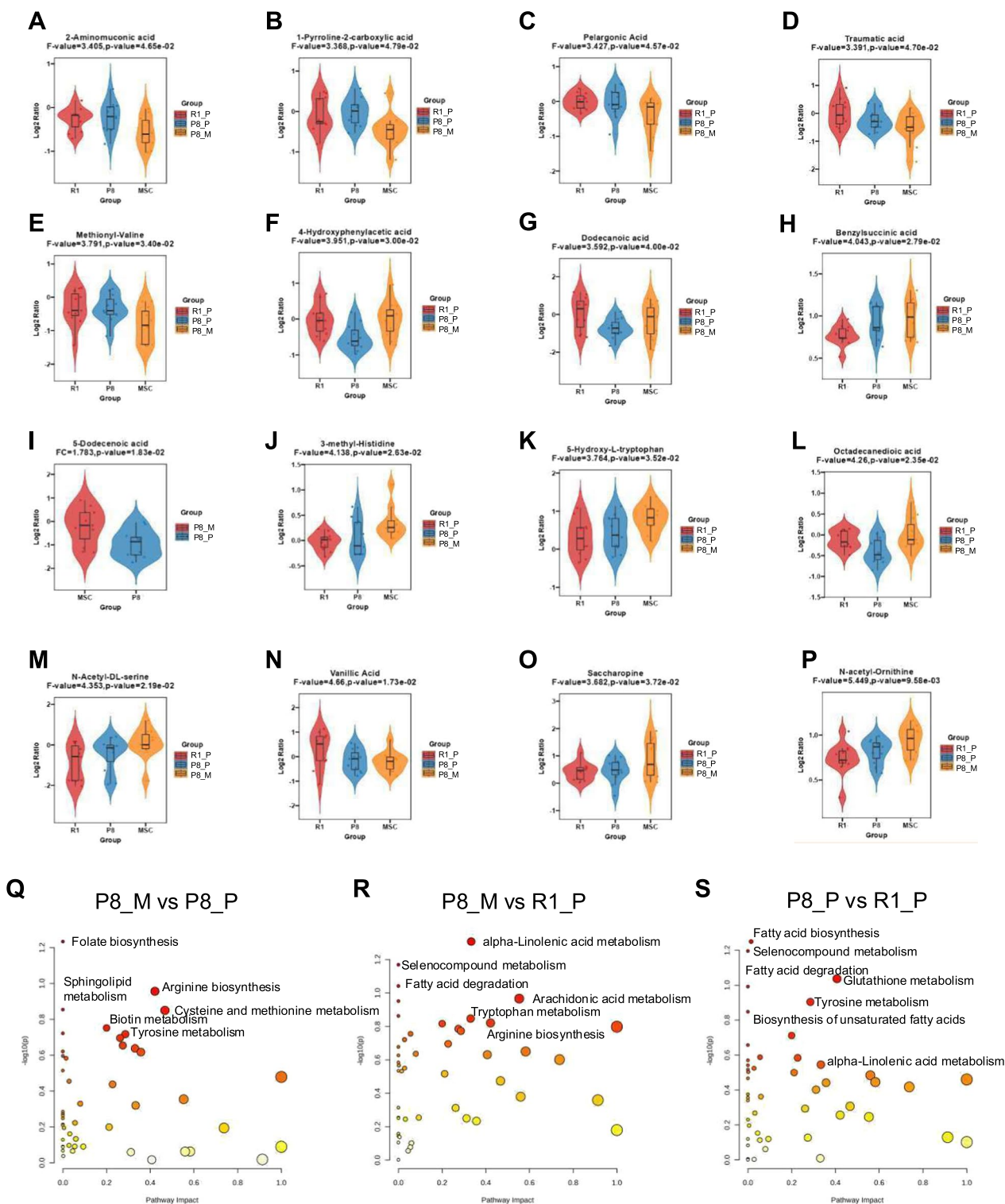


Fig. 6 (See legend on previous page.)

groups, Dodecanoic acid is negatively correlated with *Helicobacter*. Some metabolite biomarkers previously reported to increase during aging or pathological states

are negatively correlated with potentially beneficial bacteria. For instance, in the SAMP8_PBS vs SAMP8_MSC comparison groups, 2-Aminomuconic acid is negatively

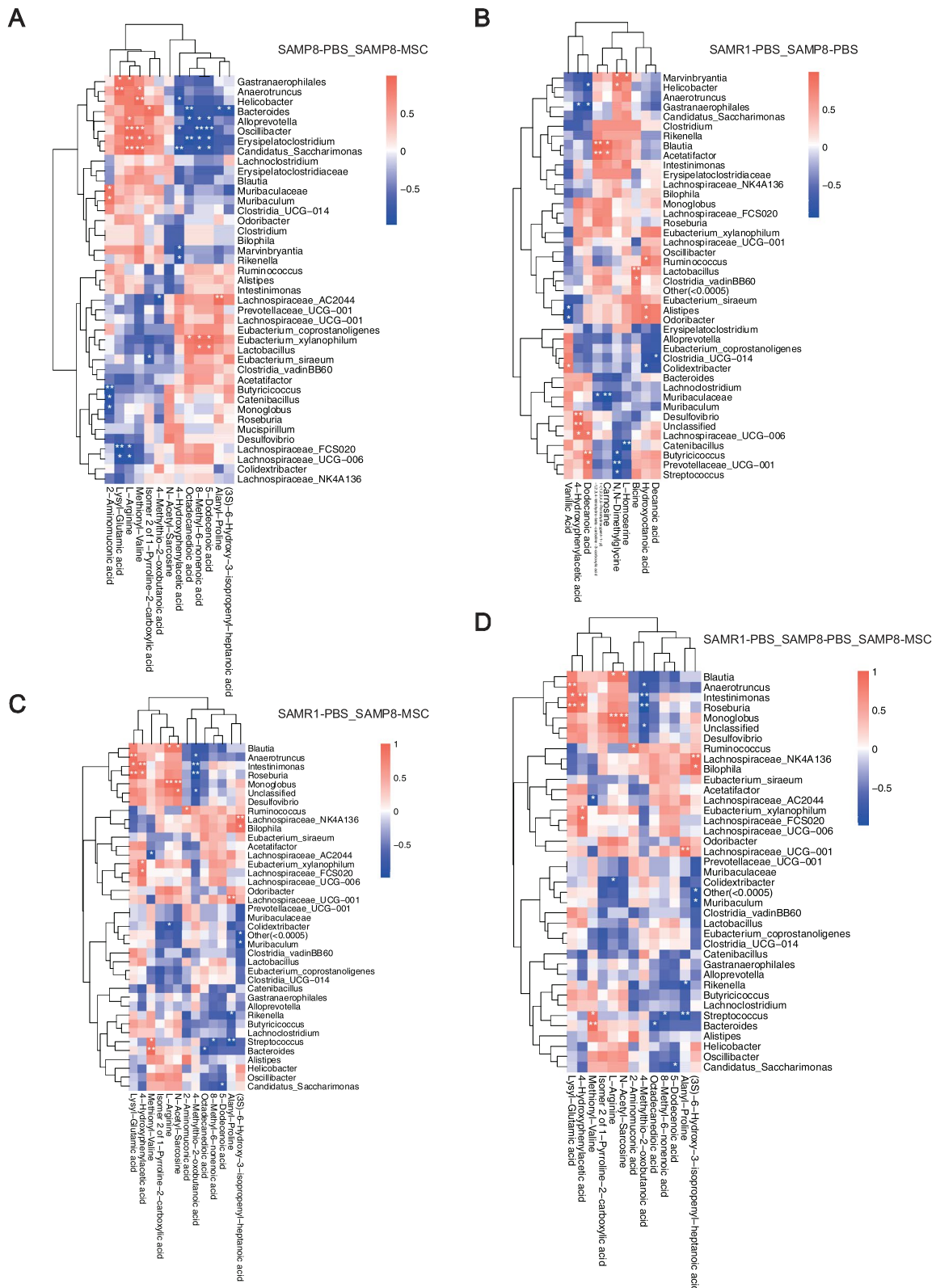


Fig. 7 Correlation Analysis between Metabolomics and Fecal Microbiota. These heatmaps display significant differences in metabolites and fecal microbiota between: **A** SAMP8_PBS and SAMP8_MSC groups. **B** SAMR1_PBS and SAMP8_PBS groups. **C** SAMR1_PBS and SAMP8_MSC groups. **D** All three groups (SAMR1_PBS, SAMP8_PBS, and SAMP8_MSC) combined. Correlations were analyzed using Spearman's method with custom R scripts. $n=3$ for each group. Significance notes: $0.001 < p < 0.01$ denoted as "***", $0.01 < p < 0.05$ denoted as "**", no notation if $p > 0.05$

correlated with *Monoglobus*, *Butyricoccus*, *Muribaculum*, *Muribaculaceae*, *Catenibacillus*, *Lachnospiraceae*_AC2044, *Prevotellaceae*_UCG-001, and *Roseburia*; Isomer 2 of 1-Pyrroline-2-carboxylic acid is negatively correlated with *Eubacterium_siraeum*. Some metabolite biomarkers previously reported to increase during aging or pathological states are positively correlated with potentially harmful bacteria. For example, in the SAMP8_PBS vs SAMP8_MSC comparison groups, Isomer 2 of 1-Pyrroline-2-carboxylic acid is positively correlated with *Erysipelatoclostridium*.

Discussion

Therapeutic potential and histopathological evidence

The findings from our study demonstrate that human umbilical cord-derived mesenchymal stem cells (HUCMSCs) can significantly ameliorate the pathological features in various organs of senescence-accelerated mouse models (SAMP8), which supports the therapeutic potential of MSCs in aging-related disorders and regenerative medicine. Our histopathological evaluations reveal that MSC treatment notably improves tissue architecture and reduces signs of aging and stress, particularly in brain, heart, kidney, muscle, lung and colon tissues (Fig. 2). Specifically, in the brain, despite the mild stress responses in the SAMP8_PBS group, the preservation of structural integrity in the frontal lobe and hippocampus in the MSC-treated groups (SAMP8_MSC) suggests a neuroprotective role of MSCs. This aligns with previous studies indicating that MSCs can exert anti-inflammatory and neuroprotective effects, potentially through the modulation of the local microenvironment or by secreting neurotrophic factors [27].

Cardiac tissue improvements were also prominent, with the maintenance of normal myocardial structures under MSC treatment. This may be associated with MSCs' ability to modulate fibrotic pathways and enhance tissue repair [28]. Additionally, improvements were observed in the lung, muscular, renal, and colonic tissues, where MSCs appeared to mitigate cellular stress and inhibit inflammatory cytokine production. These anti-inflammatory properties of MSCs are likely responsible for the preservation of tissue integrity in these organs [29].

Biological distribution of MSCs post-intraperitoneal injection

Preclinical studies have shown that intraperitoneal injection (IP) of MSCs is more effective in treating colitis than intravenous infusion. The IP route enhances MSC migration to the inflamed colon, leading to higher efficiency, improved survival rates, reduced weight loss, faster weight gain, which is consistent with the observations

in the present study [30]. When administered intraperitoneally, MSCs modulate the peritoneal microenvironment, subsequently affecting intestinal immune responses. However, fewer than 1% of MSCs reach the inflamed colon, with most BM-MSCs aggregating in the peritoneal cavity. MSC-derived factors, such as TSG6, are involved in modulating intestinal inflammatory responses, despite MSCs not directly localizing to the intestinal tissue [31]. Studies showed that human umbilical cord-derived mesenchymal stem cells (HUCMSCs) ameliorate TNBS-induced colitis by normalizing the gut microbiota, and it has been suggested that HUCMSCs ameliorate colon inflammation via modulation of the gut microbiota-SCFAs-immune axis [4, 32]. Based on existing research, we hypothesize that MSCs may not directly act on the gut microbiota but instead alter the composition and function of gut microorganisms by modulating the intestinal immune system and microenvironment. This immune-modulatory effect likely initiates changes in the gut microbiota that further impact metabolism and immune responses, creating a positive feedback loop. Furthermore, we are interested in whether MSCs, administered intraperitoneally, can improve the health of distant organs, such as the heart and brain, through systemic mechanisms involving the gut-microbiota-metabolism axis.

In the present study, intraperitoneally administered HUCMSCs in SAMP8 mice led to significant alterations in the gut microbiota, increasing beneficial SCFA-producing bacteria such as *Prevotella* and *Roseburia*, suggesting that MSCs may act on the gut microbiota. These alterations were correlated with improved metabolic profiles, enhanced cognitive function, and improved structure and function of organs such as the heart and the brain, indicating the indirect protective effects on overall health. While current findings indicate that MSCs can influence the intestinal flora through immune modulation, further studies are needed to elucidate the exact mechanisms by which MSCs regulate the microbiota. Future research should focus on identifying specific MSC-secreted factors that influence gut microbial populations and the role of immune cells in mediating these effects. Additionally, studies investigating the long-term impact of MSC treatment on gut flora composition and function will provide more insight into the therapeutic potential of MSCs in aging-related disorders. Although MSCs are known to migrate to sites of inflammation in various studies, there is a lack of systematic comparison regarding MSC biodistribution and turnover using different administration routes in different disease models. In the future, we can use in vivo imaging techniques to study the consistency of MSC distribution and

inflammation sites in different disease models, including the SAM model of accelerated aging in this study.

MSCs' mechanisms of action: anti-inflammatory, neuroprotective, and DNA repair

MSCs are known to reduce brain damage through their anti-inflammatory and anti-apoptotic properties, mainly via MSC-secreted exosomes mediated paracrine signaling [27]. Intraperitoneally administered HUCMSCs have demonstrated neuroprotective effects in Alzheimer's disease [33]. These protective effects are often attributed to the secretion of growth factors, such as hepatocyte growth factor (HGF), which promote cell survival and reduce inflammation in the central nervous system [33]. MSCs may reduce the release of neurotoxic chemokines and increase the generation of neuroprotective factors, thereby mitigating DNA damage and cell death. For instance, metabolic changes may influence DNA damage and aging-related pathways, such as NAD⁺ depletion-mediated activation of the cGAS-STING pathway in neuroinflammation and cellular senescence in Alzheimer's disease [34]. Recently, an intriguing study suggests that memory formation involves the inflammation-associated DNA-sensing TLR9 pathway and transient neuronal DNA damage [35]. We propose that MSCs' anti-inflammatory effects may alleviate the adverse consequences of this inflammation, promoting faster DNA damage-repair cycles and reducing the accumulation of irreversible harmful DNA damage in the brain.

In the present study, the application of the SSiNGLE method provided critical insights into the molecular mechanisms underlying the anti-aging effects of HUCMSCs. By mapping DNA single-strand breaks (SSBs) at a genome-wide scale, we were able to assess the extent of DNA damage in aging brain tissue. Our findings revealed that SAMP8 mice exhibited elevated levels of SSBs across the entire genome. Notably, HUCMSC treatment significantly reduced SSB levels, suggesting that MSCs may confer neuroprotective effects by mitigating DNA damage in critical genomic regions. This reduction in DNA damage aligns with the observed improvements in cognitive function and tissue integrity, indicating that the preservation of genomic stability is a key aspect of the anti-aging effects mediated by HUCMSCs. The SSiNGLE analysis thus highlights the potential of MSC-based therapies to address the molecular pathology of aging at the genomic level. Interestingly, regions with altered SSB distributions were enriched for metabolism-related genes. This indicates that MSCs might exert their neuroprotective effects by enhancing the DNA repair process in these regions, suggesting a critical role for metabolism in MSC-mediated DNA repair and neuroprotection. This finding underscores the importance of metabolism in aging and

positions it as a focal point for further investigation into MSC therapy. Future research should focus on investigating the specific molecular pathways through which MSCs protect DNA in the brain. This may involve exploring the role of growth factors such as HGF and other factors secreted by MSCs in promoting DNA repair and reducing oxidative stress. Additionally, studies should focus on isolating MSC-derived exosomes and identifying the key components responsible for DNA repair. Moreover, exploring combination therapies that enhance MSC efficacy in preventing age-related DNA damage may offer new avenues for treating neurodegenerative diseases.

Gut microbiota, metabolism, and HUCMSCs' indirect effects on overall health

Given that the administration method used in this study was intraperitoneal injection, and significant improvements were observed in tissues of organs distant from the peritoneal cavity—such as the brain, heart, lungs, and skeletal muscles—we speculate that MSCs, in addition to exerting paracrine effects on nearby intraperitoneal organs, may also modulate the intestinal microbiota. This modulation likely induces changes in metabolite profiles that influence the health of distant organs through pathways such as the gut-brain axis and the gut-heart axis. To investigate this hypothesis, we employed 16S rDNA sequencing to analyze the composition of the intestinal microbiota (Fig. 5, 6). *Prevotella* is common in plant-rich diets, it aids in the breakdown of carbohydrates and fiber [36]. *Prevotellaceae*, often considered a "probiotic" in humans, show reductions linked to conditions such as autism, allergies, and autoimmune diseases [37]. The presence of *P. Copri* in maternal stool samples correlates with a reduced risk of allergies in infants [38]. Furthermore, a deficiency of *Prevotella histicola* in patients with Multiple Sclerosis, a disease characterized by microbiota imbalances, highlights its significance [39]. Similarly, *Lachnospiraceae_AC2044*, found in the healthy human gut, synthesizes short-chain fatty acids (SCFA) through the fermentation of dietary polysaccharides, providing essential energy for intestinal cells and showing a protective role against radiation-induced damage in mice [40], reducing stress-induced visceral hypersensitivity in animal models, potentially offering a therapeutic avenue for treating conditions like irritable bowel syndrome [41]. However, some studies suggest potential harmful effects, indicating its impact may be conditional [42]. Additional research into other gut flora such as *Roseburia* reveals its critical role in producing butyric acid, enhancing colon motility and exhibiting anti-inflammatory properties [43]. *Roseburia* is positively related to longevity. A deficiency in *Roseburia* is associated with various metabolic disorders and diseases such as irritable bowel syndrome,

obesity, type 2 diabetes, neurological disorder, allergies, and liver disease [44]. In the treatment of colorectal cancer, butyrate from *Roseburia intestinalis* enhances the efficacy of immune checkpoint inhibitors by activating cytotoxic T cells, indicating its potent therapeutic potential [45]. *Roseburia* is significantly reduced in the gut microbiota of AD patients compared with the normal population [46].

In terms of metabolite changes, MSC treatment decreased several metabolites potentially harmful to health. For example: 2-Aminomuconic acid levels were notably lower in the MSC-treated group, suggesting enhanced mitochondrial function and health through the regulation of NAD⁺ synthesis [47] (Fig. 6A). Significant reductions were also observed in the levels of metabolic disorder related Isomer 2 of 1-Pyrroline-2-carboxylic acid [48] and aging related Pelargonic Acid [49] in the MSC-treated groups (Fig. 6B-C). Traumatic acid, which plays a role in regulating lipid accumulation [50], was also notably lower in the MSC-treated group, suggesting a potential reversal of age-related weight loss due to MSC-mediated improvements in lipid metabolism (Fig. 6D, Fig. 2). Additionally, MSC treatment appeared to downregulate Methionyl-Valine, a variant of the amino acid methionine (Fig. 6E). Methionine has been shown to regulate metabolic processes, oxidative stress, and diseases such as cardiovascular disorders [51]. However, excess methionine can elevate homocysteine levels, posing cardiovascular risks, though acute doses show reversible vascular dysfunction without long-term damage [52]. Interestingly, dietary Valine has been shown to impact gut health and potentially accelerate nonalcoholic fatty liver disease, underlining the complex role such amino acids play in health and disease [53]. These inconsistencies or uncertainty underscore the need for further investigation into its significant role and impact under MSC treatment.

The administration of MSCs appeared to increase several metabolites with potential health benefits. For instance, 4-Hydroxyphenylacetic acid (4-HPAA) (Fig. 6F) reduces the burden of diet-induced cardio-metabolic diseases [54] and inhibits the growth of *Clostridioides difficile*, linking it to reduced inflammation and improved gut health [55]. Although typically upregulated during infections and considered pro-inflammatory [56], there are reports suggesting potential health benefits of Dodecanoic acid (Lauric acid) (Fig. 6G). As a medium-chain fatty acid, Dodecanoic acid may be beneficial for heart health, helping to regulate lipid levels and reduce oxidative stress in the heart and kidneys^[57]. 2-Benzylsuccinic acid (Fig. 6H), known as a potent and reversible inhibitor targeting the active site of carboxypeptidase A (CPA),

has gained prominence for its role in the discovery of ACE inhibitors [58, 59]. It has been shown to help alleviate hypertension, illustrating its potential therapeutic benefits in cardiovascular health management [58, 59]. 5-dodecenoic acid was down-regulated in patients with Stable Coronary Artery Disease (SCAD) compared to health people [60]. Significantly higher levels of 5-dodecenoic acid in the SAMP8-MS group compared to the SAMP8-PBS group, indicating cardiovascular protection function exerted by MSC-metabolites regulatory axis (Fig. 6I). 3-methyl-Histidine (Fig. 6J) could offer myocardial protection during cardiac surgery [61]. These potential beneficial metabolites are vital to cardiovascular health, which is in accordance with the aligning with MSC's cardioprotective roles (Fig. 2).

Correlating the changes in gut microbiota with metabolite profiles revealed the complex interactions between specific gut microbes and metabolites. Beneficial bacteria, such as *Prevotella*, *Lachnospiraceae*, *Roseburia*, *Eubacterium xylanophilum*, *Lactobacillus* [62] and *Intestinimonas* [63], were positively associated with health-promoting metabolites. For instance, *Eubacterium xylanophilum*, a butyrate producer, promotes gut health and reduces obesity by modulating lipid metabolism [64].

On the other hand, harmful bacteria, including *Helicobacter pylori* [65], *Marvinbryantia* [42], *Rikenella* [66], and *Erysipelatoclostridium* [67], were negatively correlated with health-promoting metabolites and positively associated with aging-related metabolite markers. These findings highlight the importance of gut microbiota in mediating the health benefits of MSC treatment and the need for further research to fully elucidate these complex interactions.

Further research and limitations

Despite providing valuable data on the efficacy of early stem cell intervention in a rapid aging dementia mouse model and exploring related gut microbiota markers, this study has several limitations. First, the single sampling time may introduce bias. Samples were collected at specific time points, potentially failing to capture dynamic changes. Future studies could improve by setting multiple sampling points and extended observation period to provide a comprehensive time series and better understand the long-term effects of stem cell intervention. Second, while the SAMP8/SAMR1 animal model is widely used in aging and dementia research, its limitations should not be overlooked. SAMP8 mice, as a model for rapid aging, exhibit pathological features that differ from human dementia, which may affect the generalizability of the results. Additionally, SAMR1 mice serve as a control for normal aging but may have

unidentified differences despite their identical genetic background to SAMP8 mice, potentially impacting comparative results. Lastly, the limited sample size may affect the statistical power and reliability of the results. Future research should consider increasing the sample size and optimizing the experimental design to improve accuracy and reproducibility. In summary, while this study highlights the potential efficacy of early stem cell intervention and its impact on DNA damage, gut microbiota and metabolites, further research is needed to overcome these limitations and provide more robust mechanistic evidence.

Conclusion

The study highlights the significant therapeutic potential of clinical-grade human umbilical cord-derived mesenchymal stem cells (HUCMSCs) in ameliorating age-related pathologies in SAMP8 mice. HUCMSCs not only improved motor coordination, balance, and curiosity while reducing fear responses, but also preserved tissue integrity and mitigated pathological changes across vital organs, indicating a rejuvenating effect. Furthermore, the treatment reduced DNA single-strand breaks and revealed functional enrichment of DNA damage signals in metabolic-related genes, alongside modulating the gut microbiota to enhance microbial diversity and metabolic profiles. These findings collectively demonstrate that HUCMSCs offer a promising approach for treating age-related conditions by exerting systemic protective effects.

Supplementary Information

The online version contains supplementary material available at <https://doi.org/10.1186/s13287-024-03986-9>.

Additional file 1.
Additional file 2.
Additional file 3.

Acknowledgements

We express our gratitude to Dr. Jianxiang Zhang for his technical assistance with behavior analysis. We also acknowledge the donation of HUCMSCs from Shandong Qilu Cell Therapy Engineering Technology Co., Ltd. Additionally, we would like to thank ChatGPT-4 for its valuable assistance in refining the academic writing, which significantly enhanced the clarity, readability, and overall quality of the text.

Author contributions

The authors have made the following declarations about their contributions: ZW, FD, XL, and LX conceived and designed the experiments. JL, LX, GW, WW, PY, ML, XS, and YC performed the experiments. JL, LX analyzed the data. JL and LX wrote the paper. JL, LX, GW covered most of the experiments.

Funding

This work was supported by Xiamen Cell Therapy Research Center (Grant number: 3502Z20214001; role: design of the study, analysis, and interpretation

of data and in writing the manuscript), Key Healthcare Projects of Xiamen City (Grant number:3502Z20234008; role: design of the study), Xiamen Medical College Undergraduate Innovation and Entrepreneurship Training Program (Grant number: 202312631068; role: collection of data), Natural Science Foundation of Xiamen (Grant number: 3502Z20244ZD1009, 3502Z202372072; role: collection of data), and Health Science and Technology Project of Fujian Province (Grant number:2023QNB003; role: collection of data).

Availability of data and materials

The datasets generated during and/or analysed during the current study are available in the China National GeneBank DataBase (CNGBdb, <https://db.cngb.org/>) repository with accession number CNP0005748.

Declarations

Ethics approval

All animals were cared for in accordance with the Guide for the Care and Use of Laboratory Animals, under a protocol approved by the Laboratory Animal Management and Ethics Committee of Xiamen University (Title of the approved project: Pre-clinical study of Umbilical Cord Mesenchymal Stem Cell Therapy for Alzheimer's Disease; approval number: XMULAC20220056; date of approval: 07/04/2022).

Consent for publication

Not applicable.

Competing interests

The authors declare that they have no competing interests.

Author details

¹Xiamen Cell Therapy Research Center, The First Affiliated Hospital of Xiamen University, School of Medicine, Xiamen University, Xiamen 361003, China. ²Center for Precision Medicine, The First Affiliated Hospital of Xiamen University, School of Medicine, Xiamen University, Xiamen 361003, China. ³Department of Laboratory Medicine, The First Affiliated Hospital of Xiamen University, School of Medicine, Xiamen University, Xiamen 361003, China. ⁴Laboratory of Nutrition and Food Safety, Xiamen Medical College, Xiamen, Fujian, China. ⁵State Key Laboratory of Cognitive Neuroscience and Learning and IDG/McGovern Institute for Brain Research, College of Life Sciences, Beijing Normal University, Beijing 100875, China. ⁶Key Laboratory of Cell Proliferation and Regulation Biology, Ministry of Education, College of Life Sciences, Beijing Normal University, Beijing 100875, China. ⁷Department of Neurosurgery and Department of Neuroscience, Fujian Key Laboratory of Brain Tumors Diagnosis and Precision Treatment, Xiamen Key Laboratory of Brain Center, School of Medicine, The First Affiliated Hospital of Xiamen University, Xiamen University, Xiamen 361003, China.

Received: 8 June 2024 Accepted: 8 October 2024

Published: 29 October 2024

References

- Ren QW, et al. Incidence, clinical correlates, and prognostic impact of dementia in heart failure: a population-based cohort study. *JACC Asia*. 2023;3(1):108–19.
- Reed AL, et al. Diastolic dysfunction is associated with cardiac fibrosis in the senescence-accelerated mouse. *Am J Physiol Heart Circ Physiol*. 2011;301(3):H824–31.
- Zhang X, et al. Exosomes secreted by mesenchymal stem cells delay brain aging by upregulating SIRT1 expression. *Sci Rep*. 2023;13(1):13213.
- Liu A, et al. Human umbilical cord mesenchymal stem cells ameliorate colon inflammation via modulation of gut microbiota-SCFAs-immune axis. *Stem Cell Res Ther*. 2023;14(1):271.
- Arifin WN, Zahiruddin WM. Sample size calculation in animal studies using resource equation approach. *Malays J Med Sci*. 2017;24(5):101–5.
- Cao H, et al. Genome-wide profiles of DNA damage represent highly accurate predictors of mammalian age. *Aging Cell*. 2024;23(5): e14122.

7. He W, et al. ReSeqTools: an integrated toolkit for large-scale next-generation sequencing based resequencing analysis. *Genet Mol Res.* 2013;12(4):6275–83.
8. Schloss PD, et al. Introducing mothur: open-source, platform-independent, community-supported software for describing and comparing microbial communities. *Appl Environ Microbiol.* 2009;75(23):7537–41.
9. Lozupone C, Knight R. UniFrac: a new phylogenetic method for comparing microbial communities. *Appl Environ Microbiol.* 2005;71(12):8228–35.
10. Lozupone CA, et al. Quantitative and qualitative beta diversity measures lead to different insights into factors that structure microbial communities. *Appl Environ Microbiol.* 2007;73(5):1576–85.
11. Caporaso JG, et al. QIIME allows analysis of high-throughput community sequencing data. *Nat Methods.* 2010;7(5):335–6.
12. Lozupone C, et al. UniFrac: an effective distance metric for microbial community comparison. *ISME J.* 2011;5(2):169–72.
13. Douglas GM, et al. PICRUSt2 for prediction of metagenome functions. *Nat Biotechnol.* 2020;38(6):685–8.
14. Wang J, et al. Involvement of oxidative stress in SAMP10 mice with age-related neurodegeneration. *Neurol Sci.* 2015;36(5):743–50.
15. Li L, et al. Effect of feeding of a cholesterol-reducing bacterium, *Eubacterium coprostanoligenes*, to germ-free mice. *Lab Anim Sci.* 1998;48(3):253–5.
16. Pan LL, et al. Clostridium butyricum strains suppress experimental acute pancreatitis by maintaining intestinal homeostasis. *Mol Nutr Food Res.* 2019;63(13):e1801419.
17. Ariyoshi T, et al. Effect of *Clostridium butyricum* on gastrointestinal infections. *Biomedicines.* 2022;10(2):483.
18. Chen Y-R, et al. Desulfovibrio is not always associated with adverse health effects in the guangdong gut microbiome project. *PeerJ.* 2021;9: e12033.
19. Trøseid M, et al. The gut microbiome in coronary artery disease and heart failure: current knowledge and future directions. *EBioMedicine.* 2020;52: 102649.
20. Turner EH, Loftis JM, Blackwell AD. Serotonin a la carte: supplementation with the serotonin precursor 5-hydroxytryptophan. *Pharmacol Ther.* 2006;109(3):325–38.
21. Trowbridge J, et al. Extending nontargeted discovery of environmental chemical exposures during pregnancy and their association with pregnancy complications—a cross-sectional study. *Environ Health Perspect.* 2023;131(7):77003.
22. Vanholder R, et al. A bench to bedside view of uremic toxins. *J Am Soc Nephrol.* 2008;19(5):863–70.
23. Toyohara T, et al. Metabolomic profiling of uremic solutes in CKD patients. *Hypertens Res.* 2010;33(9):944–52.
24. Osorio-Paz I, et al. Vanillic acid improves stress resistance and substantially extends life span in *Caenorhabditis elegans*. *J Gerontol A Biol Sci Med Sci.* 2023;78(7):1100–7.
25. Zhou J, et al. The lysine catabolite saccharopine impairs development by disrupting mitochondrial homeostasis. *J Cell Biol.* 2019;218(2):580–97.
26. Huang N, et al. A pilot case-control study on the association between N-acetyl derivatives in serum and first-episode schizophrenia. *Psychiatry Res.* 2019;272:36–41.
27. Baez-Jurado E, et al. Secretome of mesenchymal stem cells and its potential protective effects on brain pathologies. *Mol Neurobiol.* 2019;56(10):6902–27.
28. White SJ, Chong JH. Mesenchymal stem cells in cardiac repair: effects on myocytes, vasculature, and fibroblasts. *Clin Ther.* 2020;42(10):1880–91.
29. Caplan AI, Dennis JE. Mesenchymal stem cells as trophic mediators. *J Cell Biochem.* 2006;98(5):1076–84.
30. Wang M, et al. Intraperitoneal injection (IP), Intravenous injection (IV) or anal injection (AI)? Best way for mesenchymal stem cells transplantation for colitis. *Sci Rep.* 2016;6:30696.
31. Sala E, et al. Mesenchymal stem cells reduce colitis in mice via release of TSG6, independently of their localization to the intestine. *Gastroenterology.* 2015;149(1):163–176.e20.
32. Yang F, et al. Human umbilical cord-derived mesenchymal stem cells ameliorate experimental colitis by normalizing the gut microbiota. *Stem Cell Res Ther.* 2022;13(1):475.
33. Jia Y, et al. HGF mediates clinical-grade human umbilical cord-derived mesenchymal stem cells improved functional recovery in a senescence-accelerated mouse model of Alzheimer's disease. *Adv Sci (Weinh).* 2020;7(17):1903809.
34. Hou Y, et al. NAD(+) supplementation reduces neuroinflammation and cell senescence in a transgenic mouse model of Alzheimer's disease via cGAS-STING. *Proc Natl Acad Sci U S A.* 2021;118(37):e2011226118.
35. Jovasevic V, et al. Formation of memory assemblies through the DNA-sensing TLR9 pathway. *Nature.* 2024;628(8006):145–53.
36. Precup G, Vodnar DC. Gut Prevotella as a possible biomarker of diet and its eubiotic versus dysbiotic roles: a comprehensive literature review. *Br J Nutr.* 2019;122(2):131–40.
37. Qiao Y, et al. Alterations of oral microbiota distinguish children with autism spectrum disorders from healthy controls. *Sci Rep.* 2018;8(1):1597.
38. Vuillermin PJ, et al. Maternal carriage of Prevotella during pregnancy associates with protection against food allergy in the offspring. *Nat Commun.* 2020;11(1):1452.
39. Jangi S, et al. Alterations of the human gut microbiome in multiple sclerosis. *Nat Commun.* 2016;7:12015.
40. Guo H, et al. Multi-omics analyses of radiation survivors identify radioprotective microbes and metabolites. *Science.* 2020;370(6516):eaay9097.
41. Zhang J, et al. Beneficial effect of butyrate-producing Lachnospiraceae on stress-induced visceral hypersensitivity in rats. *J Gastroenterol Hepatol.* 2019;34(8):1368–76.
42. Zhang JS, et al. Far-infrared therapy based on graphene ameliorates high-fat diet-induced anxiety-like behavior in obese mice via alleviating intestinal barrier damage and neuroinflammation. *Neurochem Res.* 2024;49:1735–50.
43. Nie K, et al. *Roseburia* intestinalis: a beneficial gut organism from the discoveries in genus and species. *Front Cell Infect Microbiol.* 2021;11: 757718.
44. Tamanai-Shacoori Z, et al. *Roseburia* spp: a marker of health? *Future Microbiol.* 2017;12:157–70.
45. Kang X, et al. *Roseburia* intestinalis generated butyrate boosts anti-PD-1 efficacy in colorectal cancer by activating cytotoxic CD8(+) T cells. *Gut.* 2023;72(11):2112–22.
46. Ling Z, et al. Structural and functional dysbiosis of fecal microbiota in Chinese patients with Alzheimer's disease. *Front Cell Dev Biol.* 2020;8: 634069.
47. Katsyuba E, et al. De novo NAD(+) synthesis enhances mitochondrial function and improves health. *Nature.* 2018;563(7731):354–9.
48. Applegarth Da Fau—Goodman, S.I., et al. Hyperprolinemia type II: identification of the glycine conjugate of pyrrole-2-carboxylic acid in urine. (0009-9120 (Print)).
49. Itoh T, et al. Selective detection of target volatile organic compounds in contaminated air using sensor array with machine learning: aging notes and mold smells in simulated automobile interior contaminant gases. *Sensors.* 2020;20(9):2687.
50. Gao J, et al. Traumatic acid inhibits ACSL4 associated lipid accumulation in adipocytes to attenuate high-fat diet-induced obesity. *FASEB J.* 2023;37(12): e23278.
51. Martínez Y, et al. The role of methionine on metabolism, oxidative stress, and diseases. *Amino Acids.* 2017;49(12):2091–8.
52. Garlick PJ. Toxicity of methionine in humans. *J Nutr.* 2006;136(6 Suppl):1722s–5s.
53. Jian H, et al. Dietary valine ameliorated gut health and accelerated the development of nonalcoholic fatty liver disease of laying hens. *Oxid Med Cell Longev.* 2021;2021:4704771.
54. Osborn LJ, et al. A gut microbial metabolite of dietary polyphenols reverses obesity-driven hepatic steatosis. *Proc Natl Acad Sci U S A.* 2022;119(48): e2202934119.
55. Harrison MA, et al. Production of p-cresol by decarboxylation of p-HPA by all five lineages of clostridioides difficile provides a growth advantage. *Front Cell Infect Microbiol.* 2021;11: 757599.
56. Hornburg D, et al. Dynamic lipidome alterations associated with human health, disease and ageing. *Nat Metab.* 2023;5(9):1578–94.
57. Alves NF, et al. Acute treatment with lauric acid reduces blood pressure and oxidative stress in spontaneously hypertensive rats. *Basic Clin Pharmacol Toxicol.* 2017;120(4):348–53.
58. Chung SJ, et al. Mechanistic insight into the inactivation of carboxypeptidase A by α -benzyl-2-oxo-1,3-oxazolidine-4-acetic acid, a novel type of irreversible inhibitor for carboxypeptidase A with no stereospecificity. *J Org Chem.* 2001;66(19):6462–71.

59. Cushman DW, Ondetti MA. History of the design of captopril and related inhibitors of angiotensin converting enzyme. *Hypertension*. 1991;17(4):589–92.
60. Zhong J, et al. The microbial and metabolic signatures of patients with stable coronary artery disease. *Microbiol Spectr*. 2022;10(6): e0246722.
61. Holeček M. Histidine in health and disease: metabolism, physiological importance, and use as a supplement. *Nutrients*. 2020;12(3):848.
62. Yin Y, et al. *Lactobacillus plantarum* GX17 benefits growth performance and improves functions of intestinal barrier/intestinal flora among yellow-feathered broilers. *Front Immunol*. 2023;14:1195382.
63. Meng C, et al. Gut microbiome and risk of ischaemic stroke: a comprehensive Mendelian randomization study. *Eur J Prev Cardiol*. 2023;30(7):613–20.
64. Wei J, et al. Dietary polysaccharide from enteromorpha clathrata attenuates obesity and increases the intestinal abundance of butyrate-producing bacterium, eubacterium xylanophilum, in mice fed a high-fat diet. *Polymers (Basel)*. 2021;13(19):3286.
65. Hooi JKY, et al. Global Prevalence of Helicobacter pylori Infection: Systematic Review and Meta-Analysis. *Gastroenterology*. 2017;153(2):420–9.
66. Sun H, et al. Selenized glucose improves rat semen quality by improving the gut microbiota and serum metabolome. *Food Funct*. 2023;14(11):5105–19.
67. Ning L, et al. Microbiome and metabolome features in inflammatory bowel disease via multi-omics integration analyses across cohorts. *Nat Commun*. 2023;14(1):7135.

Publisher's Note

Springer Nature remains neutral with regard to jurisdictional claims in published maps and institutional affiliations.